International Journal of Heat and Mass Transfer 169 (2021) 120962

Contents lists available at ScienceDirect

International Journal of Heat and Mass Transfer

journal homepage: www.elsevier.com/locate/hmt

Maxwell's equations explain why irreversible electroporation will *not* heat up a metal stent

Cees W.M. van der Geld[a,*], Ruben T. van Gaalen[b], Hester J. Scheffer[c], Jantien A. Vogel[d], Willemien van den Bos[e], Martijn R. Meijerink[c], Marc G.H. Besselink[d], Rudolf M. Verdaasdonk[f,*], Martin J.C. van Gemert[g]

[a] Department of Chemical Engineering and Chemistry and Chemical Engineering, Eindhoven University of Technology, Eindhoven, the Netherlands
[b] Department of Mechanical Engineering, Eindhoven University of Technology, Eindhoven, the Netherlands
[c] Departments of Radiology and Nuclear Medicine, Free University Medical Center, Amsterdam, the Netherlands
[d] Department of Surgery, Cancer Center Amsterdam, Amsterdam UMC, University of Amsterdam, Amsterdam, the Netherlands
[e] Department of Radiology, Amsterdam UMC, University of Amsterdam, Amsterdam, the Netherlands
[f] TechMed Center, Faculty of Sciences, University of Twente, Enschede, the Netherlands
[g] Department of Biomedical Engineering and Physics, Academic Medical Center, University of Amsterdam, Amsterdam, the Netherlands

ARTICLE INFO

Article history:
Received 28 September 2020
Revised 23 December 2020
Accepted 8 January 2021

Keywords:
Irreversible electroporation
Electric field
Heat conduction
Stent

ABSTRACT

Irreversible Electroporation (IRE) is a promising clinical ablation therapy for the treatment of cancer, but issues with the generation of heat must be solved before safe and effective clinical results can be obtained. In the present study, we show that a metal stent will *not* be noticeably heated up by IRE pulses under typical clinical conditions. Derivation of this non-intuitive result required the application of Maxwell's equations to the tissue-stent configuration. Subsequently, straightforward and arguably accurate simplifications of the electric field generated by two needles in tissue surrounding a metal stent have enabled the modeling of the heat generation and the transport of heat in IRE procedures. Close to a stent that is positioned in between two needles, temperatures in a typical run of 100 s, 1 Hz pulses, may remain notably lower than without the stent. This is the explanation of the experimentally observed low temperature rim of viable tissue around the stent, whereas all tissue was non-viable without stent, found in tissue model experiments.

1. Introduction

Irreversible Electroporation (IRE) is a promising clinical ablation therapy for the treatment of cancer, in particular when tumors are located near vulnerable structures. The technique utilizes high-voltage, about 90 microsecond electrical pulses that are applied through needle electrodes that are positioned in the tumor. The electrical pulses have a maximum voltage in the range 1000 to 1500 V and current in the range 15 to 35 A. The electrical pulses destabilize the existing transmembrane potential over the membrane boundary of cancer cells and lead to the formation of so-called 'nano-pores' in the cellular membrane. Due to the resulting increased cell membrane permeability, the cell loses its normal properties and cell death results [1–3]. Cells are killed in a targeted region, without damaging the collagen and other interstitial tissue constituents. This localized treatment makes it possible to preserve critical structures, like major vasculature and ductal systems [3–5]. This sparing of critical structures is the primary characteristic that distinguishes IRE from other local therapies [4]. The clinical procedure with IRE is with two or more needles within close distance (order of 5 mm) of each other to keep the electric field localized and generally requires about 100 pulses at 1 Hz. The two needles are usually in parallel; reference [5] gives figures of this and other needle geometries.

The underlying physics of IRE is complex and still incompletely understood. An important example is that IRE received strong scientific and industrial marketing, arguing that tissue cell death occurs only by nanopores in the cell membranes created by short and intense IRE electric pulses [1,2], and that the inevitable Joule heating developing when a voltage is applied between electrodes placed in an electric conducting tissue can be kept sufficiently limited [3,4,6]. Controversy then developed concerning possible thermal effects of IRE. First, IRE, as currently applied in clinical proce-

* Corresponding authors.
E-mail address: C.W.M.v.d.Geld@tue.nl (C.W.M. van der Geld).

https://doi.org/10.1016/j.ijheatmasstransfer.2021.120962

Nomenclature

Roman symbols

a	radius of the stent; m
$\boldsymbol{B}$	magnetic field vector; tesla
c	heat capacity of tissue; J/(kg ^{0}C)
D	diameter of the needles; m
$\boldsymbol{D}$	electric field vector inside material; coul/m^2
$\boldsymbol{E}$	electric field vector outside of material; V/m
E_i	incident electric field component; V/m
E_r	reflected electric field component; V/m
E_t	transmitted electric field component; V/m
H_i	incident magnetic field component; ampere-turn per m
H_r	reflected magnetic field component; ampere-turn per m
H_t	transmitted magnetic field component; ampere-turn per m
f	frequency; Hz
G	Green's function
$\boldsymbol{H}$	magnetic field vector inside material; ampere-turn per m
$\boldsymbol{J}$	electric current density; amp/m^2
L	typical length scale, m
L_1	needle distance from origin, m
q	free charge density; coul/m^3
Q	electric charge; coul
r	radial position; m
$\hat{r}_i$	unit vector in direction of vector $\mathbf{r}_i$, with i a positive integer; m
t	time; s
T	temperature; ^{0}C
$T_0(x,y,z)$	initial temperature profile; ^{0}C
V	volume; m^3
x	coordinate in x-direction; m
y	coordinate in y-direction; m
z	coordinate in z-direction; m
z_1	needle coordinate in z-direction, being half the distance between two needles; m

Greek symbols

α	heat diffusivity; $\alpha = \lambda\ /(\rho\ c)$, m^2/s
Δt	typical duration of an electric pulse, s
ε	dielectric permittivity; $\varepsilon = \varepsilon_r\ \varepsilon_0$
ε_0	dielectric permittivity of vacuum; farad per m, $\varepsilon_0 = 8.854.\ 10^{-12}$
ε_r	relative permittivity; farad per m
λ	thermal conductivity; W/(m ^{0}C)
μ_0	magnetic permeability of vacuum; $\mu_0 = 4\pi.10^{-7}$ henry/m
ρ	mass density; kg/m^3
τ	time; second, s
σ	electrical conductivity; siemens per meter, $1/(\Omega.\text{m}) = \text{S/m}$
φ	angle between unit vectors; $\hat{r}_1 \cdot \hat{r}_2 = cos\varphi$
Φ	voltage; V

Acronyms

2D	two-dimensional
3D	3-dimentional
IRE	Irreversible Electroporation
Fo	Fourier number, Fo $= \alpha\ t/L^2$
LHS	left-hand-side
RHS	right-hand-side

dures, has now a proven strong Joule heating thermal part [5–13]; despite that, many recent publications still ignore mentioning this mechanism, e.g. [14,15]. A second example is that a metal device between the electrodes during IRE pulsing, *e.g.* a metal stent in the common bile duct during IRE palliation of a pancreas carcinoma, was considered a contraindication for an IRE procedure because of the intuitive assumption that the metal would be heated up [16], which was questioned by our group in a comment to that publication [17,18]. Nevertheless, it was recently still mentioned that a metal stent is a contraindication for IRE [14]. Whether a metal stent is indeed a contraindication for therapy and needs to be removed prior to application of IRE or not is of utmost importance as it may withhold a patient from relevant therapy while surgical removal can be associated with complications. Convincing proof of non-heating of the metal stent is therefore essential. This study, the physics part of the joint efforts between clinicians and physicists, to understand clinically relevant IRE issues, aims at delivering this proof by a theoretical approach. The governing Maxwell and bioheat equations and boundary conditions will be shown to allow for simplifications that yield straightforward and relatively easy computations. The Green's function method to account for heat conduction [20] will be exploited and full profit will be taken of the additivity of temperature solutions of the heat equation. Matlab^{TM} is used as a high-level language for the actual computations. Comsol^{TM} computations have been used for validation of the simplifications applied.

Laboratory experiments have been carried out to examine the development of temperature fields in human-like tissue, in jelly phantoms and in porcine experiments, due to electric heating with needles [12,13]. One unexpected finding was that temperatures in the vicinity of a stent were *lower* than at the same location without a stent. The present study will explain this experimental finding and will elucidate the trends found in these experiments.

The aims of our paper are:

1 to model the thermal behavior of IRE procedures without and with a metal stent between two needles that generate an electric field;
2 to prove with the use of Maxwell's equations that metal stents hardly increase in temperature in response to a clinical IRE pulse;
3 to explain thermo-camera experiments in [12,13].

The organization of the paper is as follows. Governing equations, boundary conditions, simplifications and approximation methods are explained in Section 2. Results and comparison with experiments are presented in Section 3. Conclusions are given in the final section. Two appendices provide details of some results.

2. Methods

2.1. Governing equations and temperature solution

2.1.1. Maxwell's equations and electric heat production

Although the governing equations are well known, they are summarized below to introduce symbols and units as well as the conditions under which simplifications are allowed.

Let the dielectric permittivity of a material be given by $\varepsilon = \varepsilon_r\ \varepsilon_0$, where ε_r denotes the dimensionless *relative* dielectric permittivity of a material and ε_0 the dielectric permittivity in vacuum; $\varepsilon_0 = 8.854.\ 10^{-12}$ farad/m. With $\boldsymbol{E}$ the electric field vector outside of material in V/m (volt/m), the electric field vector including polarization inside material, $\boldsymbol{D}$, in coul/m^2 (coulomb/m^2) is given by

$$\mathbf{D} = e\mathbf{E}. \tag{1}$$

The magnetic field without polarization, $\boldsymbol{B}$, in tesla is expressed in the one with polarization, $\boldsymbol{H}$, in ampere-turn per m via

$$\mathbf{B} = \mu_0(\mathbf{H} + \mathbf{M}), \tag{2}$$

where μ_0 is the magnetic permeability of vacuum that amounts $4\pi.10^{-7}$ henry/m.

Finally, let Q denote a free point charge at a point in coul (coulomb), let q denote free charge density in coul/m^3 and let $\boldsymbol{J}$ be the time rate of change of charge, which is equal to the electric current density in amp/m^2 (ampere/m^2). The Maxwell equations read [20]:

$$\nabla.\mathbf{D} = q \tag{3}$$

$$\nabla.\mathbf{B} = 0 \tag{4}$$

$$\nabla \times \mathbf{H} = \mathbf{J} + \partial\,\mathbf{D}/\partial t \tag{5}$$

$$\nabla \times \mathbf{E} = -\partial\mathbf{B}/\partial t. \tag{6}$$

The continuity equation for charge and current is the following:

$$\nabla.\mathbf{J} = -\partial\, q/\partial t. \tag{7}$$

The symbol σ denotes the specific conductivity in $1/(\Omega.\mathrm{m})$ = S/m (Siemens/m). Ohm's law, $\boldsymbol{J} = \sigma\ \boldsymbol{E}$, holds for quasi-steady processes and is a simplification of the following general expression for the electric current, which is the essential generalization of previous versions found by Maxwell [20, page 218]:

$$\mathbf{J} = \sigma\,\mathbf{E} + \partial\,\mathbf{D}/\partial t. \tag{8}$$

For free charges, current density is given by $\boldsymbol{J} = \sigma\ \boldsymbol{E}$, which is Ohm's law. With the equation of continuity, $\partial q/\partial t + \nabla.\boldsymbol{J} = 0$, it is easily seen that a typical response time of free charges is given by $\tau = \varepsilon\ /\sigma$. The derivation requires assuming ε and σ to be homogeneous and substitution of $q = exp(-t/\tau)$ in the combination of $\partial q/\partial t = -\nabla.\boldsymbol{J}$ and $\nabla\ .\boldsymbol{J} = \sigma\ q/\varepsilon$. Let Δt be a typical duration of an electric pulse used for current clinical IRE procedures. If the response time τ is small with respect to Δt, then electric currents are quasi-stationary, which implies that $\boldsymbol{n}_2.(\boldsymbol{J}_1 - \boldsymbol{J}_2) = 0$, where $\boldsymbol{n}_2$ is the outward normal to volume numbered 2 and $\boldsymbol{J}_1$ and $\boldsymbol{J}_2$ are the current densities on both sides of the volume boundary where the normal is positioned. For a metal, typical values are $\sigma\ \sim 10^7$ S/m and $\varepsilon_{\ r} = 1$. This means that $\tau\ \sim 10^{-18}$ s $<<\ \Delta\ t \sim 10^{-4}$ s. During a typical IRE pulse, electric currents can thus be considered as stationary.

If an electric field is rapidly changing, as for example during the switching on and off of electric potentials, an electric field might be generated that may penetrate into a metal shield. In that case the full Maxwell equations must be considered. This will be done below, in Section 2.3, for the standard conditions of IRE. In actual conductors, the fields are attenuated exponentially in a characteristic length, which is called the skin depth. The amount of attenuation in the skin depth will be quantified for clinical conditions to justify the assumption of quasi-steady in the computational results of Section 3.

If the conditions determining electric fields are quasi-steady, there is no need to solve for the magnetic field; in that case $\nabla\ .\ \boldsymbol{J} = 0$. For a homogeneous electric conductivity, the last equation of a divergence-free current in combination with the defining equation of the electric potential, Φ, in volt:

$$\mathbf{E} = -\nabla \cdot \Phi \tag{9}$$

yields the Laplace equation $\nabla.\nabla\ \Phi = 0$. This is the equation of electrostatics that will be employed to compute the electric field under conditions prevailing in clinical IRE procedures.

The time rate of change of mechanical energy in a volume V is given by

$$\int_V \mathbf{J}.\mathbf{E}\,dV \tag{10}$$

The energy dissipation rate density of electric fields, the conversion rate of electric energy to heat per unit of volume, in W/m^3, is with Ohms law therefore given by $\sigma\ \boldsymbol{E}^2$. This heat production leads to temperature changes that are computed in the way described in the following section.

2.1.2. IRE temperatures calculated with Green's functions and modeling assumptions

The bioheat equation for the partial derivative with respect to time, t, of the temperature, T, in tissue exposed to an electric field, E, and of mass density, ρ, (kg/m^3), heat capacity, c, (J/kg/°C), electric conductivity, σ, and thermal conductivity, λ (W/m/°C) is, e.g. [10]

$$\rho c\frac{\partial T}{\partial t} = \sigma E^2 + \lambda\nabla^2 T. \tag{11}$$

Let $T_0(x,y,z)$ be the initial temperature profile. Heat diffusion and the generation of heat occur, that both modify the spatial initial temperature profile. Heat diffusion is here calculated by a Green's function approach [19]. Initial temperature profile T_0 is usually taken homogeneous and equal to 37°C, which will be taken as the reference temperature field from now on.

Let the thermal diffusivity be $\alpha = \lambda/(\rho c)$. The clinical IRE needles usually generate electricity over a great part of their length. End effect will be ignored and the heat generation takes the form of a line source in that case, which makes the computational domain essentially two-dimensional. Green's functions exist for finite domains, but in this study spreading of heat during 100 s at maximum will be considered. The typical length scale, L, of spreading of heat from a source is estimated by putting the Fourier number, $\mathrm{Fo} = \alpha\ t\ /\ L^2$, equal to 1. For a heat diffusivity of $1.4\ \cdot\ 10^{-7}$ m^2/s and a time of 100 s, L is easily found to be approximately 4 cm.

The IRE treatment therefore remains localized in a small spatial domain as compared to the dimensions of the human body. It is therefore safe to assume that the heat produced can diffuse freely without being affected by boundaries and to adopt Greens' functions for an infinite body.

For an IRE geometry of two parallel needle electrodes of infinite length in the y-direction, a Cartesian coordinate system (x, z) and time t will be employed. The needles point in the y-direction, the z-axis joins the centers of the needles and the x-axis is normal to the origin that is located in between the two needles (Fig. 1). The thermal diffusion from an infinite unit line source occurring instantaneously at position x', z' and time τ is conveniently described by the following Green's function [19]:

$$G\left(x,z,t;x',z',\tau\right)\ = \frac{1}{4\pi\alpha\,(t-\tau)}\cdot exp\left(-\frac{\left(x-x'\right)^2+\left(z-z'\right)^2}{4\alpha\,(t-\tau)}\right). \tag{12}$$

When the initial temperature is uniform and equal to T_0, the temperature field is given by

$$T(x,z,t) - T_0 = \int_0^t d\tau \int_{x_1}^{x_2} dx' \int_{z_1}^{z_2} dz' \frac{\sigma E\left(x',z'\right)^2}{\rho c} G\left(x,z,t;x',\ z',\ \tau\right) \tag{13}$$

where the boundaries of the integral have been chosen sufficiently large and of the order of $L = 4$ cm to make the values of either the

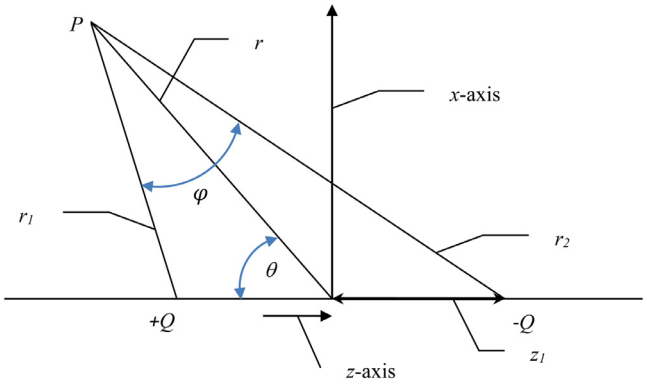

Fig. 1. Coordinates without a stent. Definition of polar angle θ and radial distances r, r_1 and r_2; the spherical needles with diameter D are represented by point charges Q and -Q.

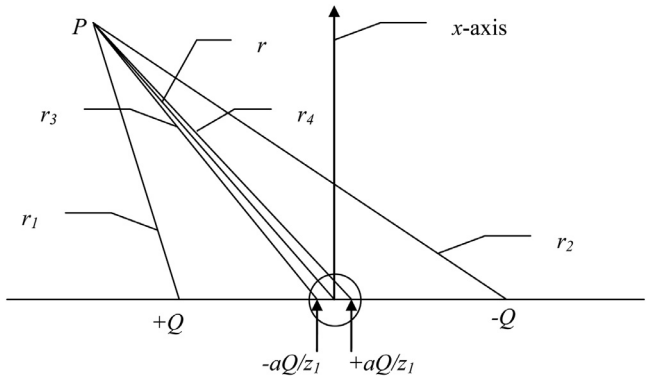

Fig. 2. Coordinates with a spherical stent. Definition of image point charge sources $\pm$ aQ/z_1 at distances $\pm$ a^2/z_1 from the center and distances r_3 and r_4 from the selected point P. The circle around the center indicates a spherical stent that has radius a. The potential of the stent surface is homogeneous with value zero.

field E or the Green's function G negligibly small at these boundaries. The heat generated at each location *(x',z')* is in (13) seen to possibly contribute to the temperature increase at the arbitrarily chosen point *(x,z)*. The double spatial integral in (13) expresses the additivity of the solutions of the energy Eq. (11) and simply sums the temperature contributions from all other places after the time the heat generation started (t=0).

The method of time partitioning is applied [19, page 167], which introduces a time t_p that satisfies $t_p < 0.025\ L^2 / \alpha$, with length L equal to the smallest characteristic length of the problem at hand [19, page 176]. The Green's function (13) in the limit for $(t - \tau)$ to zero, *i.e.* for τ in the range $(t\text{-}t_p,\ t]$ with t_p very small, becomes a product of two delta functions: $\delta(x - x').\delta(z - z')$. As a consequence,

$$T(x,z,t) - T_0 = \frac{\sigma t_p E(x,z)^2}{\rho c} + \int_0^{t-t_p} d\tau \int_{x_1}^{x_2} dx' \int_{z_1}^{z_2} dz' \frac{\sigma E\left(x',z'\right)^2}{\rho c} \times G\left(x,z,t;x',\ z',\ \tau\right). \tag{14}$$

Physically, Eq. (14) means that the contribution to the temperature rise on location *(x,z)* from the electric pulse from another place, *x'*, takes at least t_p s to diffuse towards the location *(x,z)*. The electric pulses from all places with a nonzero electric field during time interval *[0, t_p)* contribute via the integral on the RHS of Eq. (14) to the temperature rise at time t at location *(x,z)*.

Both the number of mesh points in the integration and the time t_p have been varied for typical electric fields generated by two needles (diameter, D, 1 mm) and a heat diffusivity, α, of 1.4 $\cdot$ 10^{-7} m^2/s. A first estimate based on the criterion $t_p < 0.025\ L^2 / \alpha$, with $L = 0.1D$, yields a t_p of about 1 ms. A comparison is made with results obtained without time partitioning and in all cases a value of t_p of 0.3 ms gave excellent agreement. In computations below, an electric field will be considered that is constant and nonzero during 0.1 ms and zero afterwards. Such very short electric pulses with a duration Δt, of 0.1 ms, are typical for current clinical IRE procedures At times exceeding the pulse duration of 0.1 ms the temperature increase at location *(x,z)* is well approximated by $0.0001\sigma\ E(x,z,t=0.1\ ms)^2\ /(\rho\ c)$ in that case.

Eq. (14) makes it clear that electric field histories must be computed, at first for quasi-steady conditions. This is done in Section 2.2.

2.2. IRE electric field distribution in tissue with and without a stent

It is quite convenient and straightforward to predict the electric field produced between electrodes in IRE applications by means of local charges and mirror-charges to satisfy the boundary conditions. The case without a stent is treated first.

2.2.1. Without stent

The electric field vector distribution in tissue, $E(r,\theta)$, at point $P(r,\theta)$, defined at radial coordinate r and angle θ with the horizontal z-axis (Fig. 1), caused by 2 electric point charges, $+Q$ at the left and $--Q$ at the right, both at distance z_1 from the origin, is given by

$$E(r,\theta) = \frac{Q}{4\pi\varepsilon_0}\left[\frac{\hat{r}_1}{r_1^2} - \frac{\hat{r}_2}{r_2^2}\right] \tag{15}$$

where $\hat{r}_1, \hat{r}_2$ are the unit vectors in the directions between P and Q and P and $-Q$ respectively (Fig. 1). The temperature increase distribution relates to the energy dissipation rate density, in W/m^3, that is given by the product of the electrical conductivity, σ, and the electric field squared:

$$\sigma E(r,\theta)^2 = \frac{\sigma Q^2}{(4\pi\varepsilon_0)^2}\left[\frac{\hat{r}_1}{r_1^2} - \frac{\hat{r}_2}{r_2^2}\right]^2 = \sigma\left(\frac{Q}{4\pi\varepsilon_0}\right)^2 \cdot \left[\frac{1}{r_1^4} + \frac{1}{r_2^4} - 2\frac{\hat{r}_1 \cdot \hat{r}_2}{r_1^2 r_2^2}\right]. \tag{16}$$

The vector product $\hat{r}_1 \cdot \hat{r}_2 = cos\varphi$, with φ the angle between $\hat{r}_1$ and $\hat{r}_2$. Simple expressions for this angle and for the volumetric heat production rate, $P(r,\theta) = \sigma E(r,\theta)^2$, are derived in Appendix A. This heat production will be needed to compute temperature histories.

Factor $Q/(4\pi\varepsilon_0)$ follows from the voltage potential, Φ, at arbitrary point P. For the above configuration of two point charges it is given by

$$\Phi(r,\theta) = \frac{Q}{4\pi\varepsilon_0}\left[\frac{1}{r_1} - \frac{1}{r_2}\right], \tag{17}$$

expressing that $-\nabla\Phi = \mathbf{E}$. Ways to determine $Q/(4\pi\varepsilon_0)$ when a given voltage V is put over the two electrodes will be presented for the 2D case in Section 2.2.2. Note that the needles in the present section have a 3D, spherical, shape. Because of the external charge of the other needle the voltage at the surface of a needle is inhomogeneous, whereas it should be constant as the electric field inside a conductor is zero. This can be solved by image charges in a way presented in Section 2.2.2 for the 2D case.

2.2.2. With stent

When a hypothetical stent would be a metal wire mesh with a spherical shape and radius a it could be placed in between point charges Q and $-Q$ on the z-axis (Fig. 2). There are two image charges needed inside the metal to keep the potential of the stent zero, see *e.g.* the classic text on electrodynamics by Jackson [20],

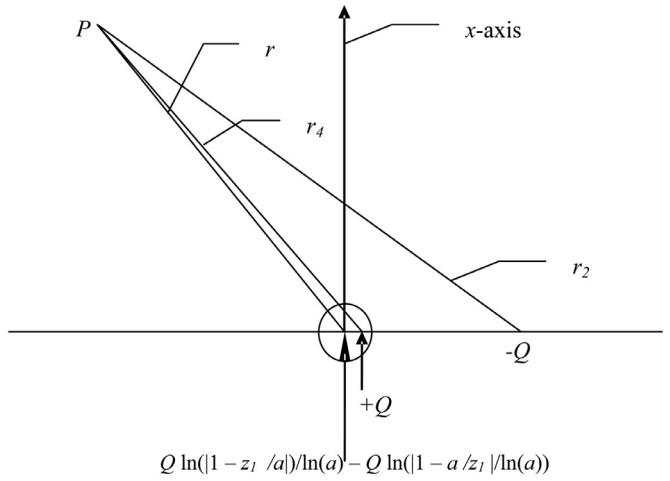

Fig. 3. Coordinates with a cylindrical stent. Definition of image line charge sources at the origin and at distance a^2/z_1 (z1/2 is the distance of charge -Q to the origin) from the center and distances r and r_4 from the selected point P. The circle around the center indicates a cylindrical stent that has radius a. The potential of the stent surface is homogeneous with value zero.

Section 2.5, Fig. 6.6. These image charges are valued $-aQ/z_1$ and aQ/z_1 and are positioned at distances $z = \pm a^2/z_1$ from the origin, see Fig. 2.

For the case depicted in Fig. 2 the electric field is composed of four contributions that can be added because the governing Laplace equation, $\Delta\Phi = 0$, is linear in the potential:

$$E(r,\theta) = \frac{Q}{4\pi\varepsilon_0}\left[\frac{\hat{r}_1}{r_1^2} - \frac{\hat{r}_2}{r_2^2} - \frac{a}{z_1}\cdot\frac{\hat{r}_3}{r_3^2} + \frac{a}{z_1}\cdot\frac{\hat{r}_4}{r_3^2}\right]. \tag{18}$$

For all points P outside of the spherical metal stent, the heat production is given by

$$\sigma E(r,\theta)^2 = \frac{\sigma Q^2}{(4\pi\varepsilon_0)^2}\left[\frac{\hat{r}_1}{r_1^2} - \frac{\hat{r}_2}{r_2^2} - \frac{a}{z_1}\cdot\frac{\hat{r}_3}{r_3^2} + \frac{a}{z_1}\cdot\frac{\hat{r}_4}{r_3^2}\right]^2 = \frac{\sigma Q^2}{(4\pi\varepsilon_0)^2}$$
$$\left[\frac{1}{r_1^4} + \frac{1}{r_2^4} - \frac{2\hat{r}_1\cdot\hat{r}_2}{r_1^2 r_2^2} + \left(\frac{a}{z_1}\right)^2\left\{\frac{1}{r_3^4} + \frac{1}{r_4^4} - \frac{2\hat{r}_3\cdot\hat{r}_4}{r_3^2 r_4^2} - \frac{2\hat{r}_1\cdot\hat{r}_3}{r_1^2 r_3^2} - \frac{2\hat{r}_1\cdot\hat{r}_4}{r_1^2 r_4^2} - \frac{2\hat{r}_2\cdot\hat{r}_3}{r_2^2 r_3^2} - \frac{2\hat{r}_2\cdot\hat{r}_4}{r_2^2 r_4^2}\right\}\right]. \tag{19}$$

Simple expressions for the RHS of the above equation are obtained with the aid of expressions such as (A3) derived in Appendix A.

A similar approach is followed for the case of two infinitely long cylindrical needle electrodes and an infinitely long cylindrical stent in between these two needles. The integral of Eq. (17) in the y-direction yields the 2D- equivalent of (17) in the form

$$\Phi(r,\theta) = \frac{Q}{4\pi\varepsilon_0}[\ln(r_1) - \ln(r_2)]. \tag{20}$$

However, because of the 3D spherical shape of the stent of Fig. 2 the image charges in the stent cannot be integrated. The solution for the 2D case of Fig. 3, with a single charge $-Q$ on the z-axis at point $z = z_1$, is the following potential:

$$\Phi(z,x,z_1)\,/V = \ln(r_4) - \ln(r_2) + [\ln(|1 - z_1/a|) - \ln(|1 - a/z_1|)]\ln(r), \tag{21}$$

where $V = \frac{Q}{4\pi\varepsilon_0}$, $r = (z^2+x^2)^{½}$, $r_4 = ((z - a^2/z_1)^2+x^2)^{½}$, $r_2 = ((z - z_1)^2+x^2)^{½}$. The potential for the case of two charges, $-Q$ at point $z = z_1$ and Q at point $z = -z_1$, that has zero value at the surface of the stent is given by

$$\Phi(z,x) = \Phi(z,x,z_1) + \Phi(z,x,-z_1)\,. \tag{22}$$

The last term on the RHS of (21) is a source term at the origin (0,0) needed to make the value of the potential at surface of the stent equal to zero. The second term on the RHS of (21), $-\ln(r_2)$, gives the needle at $z = z_1$ the desired potential, V_0, if V is appropriately chosen:

$$V = V_0/\left[\ln\left(z_1 - \tfrac{D}{2} - a^2/z_1\right) - \ln\left(\tfrac{D}{2}\right) - s\right] \quad \text{with } s = \left[\ln\left(\left|1 - \tfrac{z_1}{a}\right|\right) - \ln\left(\left|1 - \tfrac{a}{z_1}\right|\right)\right]\ln\left(z_1 - \tfrac{D}{2}\right)/\ln(a) \tag{23}$$

where D is the needle diameter. With this choice, the voltage at the needle has the desired value at only one point on the needle surface, namely at the point facing the other needle. At other points on the surface the voltage will be slightly off because of the presence of the other needle. This can be compensated with an image charge in the needle in a way described below. Because of symmetry two image charges are needed, for each needle one. With these two image charges, the voltage at a needle surface is made inhomogeneous by the image charge at the other needle. Consequently, new image charges are needed to make the potential homogeneous despite the image charge, etc. An infinite array of image charges is thus created if two needles are in proximity. In practice, needle distance is that large that only one image charge suffices to get an accurate representation of the electric field in between two needles, as will be shown below. Alternatively, the shape of the needle corresponding to one image charge can be taken not to be circular but given by the equipotential plane through the point facing the other needle. This shape will be close to being spherical with deviations negligible for all practical purposes, while the boundary conditions are now satisfied at the stent and at both needles.

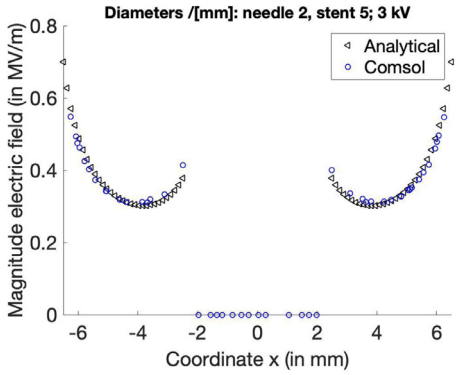

Fig. 4. Electric field strength, in unit MV/m, created in between stent and needles along the axis through the center (y=0). Needle diameter D = 2 mm; needle distance 12.5 mm, a = 2.5 mm, V_0 = 1500 V. The analytical solution is given by Eq. (21).

The strength of the image source of the needle in the stent, the first term on the RHS of (21), $\ln(r_4)$, is also V whereas in the above spherical case the strength of the images source was reduced by a factor a/z_1, Eq. (18).

The potential $\Phi(z,x)$ is anti-symmetrical with respect to the x,z-plane given by points where $y = 0$ since one needle has voltage V_0 while the other has voltage $-V_0$,. The potential at the stent surface is constant and this constant must be zero since $\Phi(a,0) = -\Phi(-a,0)$. This means that the potential is given by

$$\Phi(z,x)\,/V = \ln(r_4) - \ln(r_2) - \ln(r_3) \mp \ln(r_1), \tag{24}$$

with V given by Eq. (23) with $s = 0$. The monopoles at the origin, corresponding to the last term on the RHS of (21), $[\ln(|1 - z_1/a|) - \ln(|1 - a/z_1|)]\ln(r)$, are compensating one another.

The analytical solution of (21) is compared with the solution of Comsol™ in Fig. 4 for a distance of only 4 mm between a needle with a diameter of $D = 2$ mm and a stent with a diameter of 5 mm. A good agreement is found, considering the fact that the Comsol solution is clearly asymmetrical and with some scat-

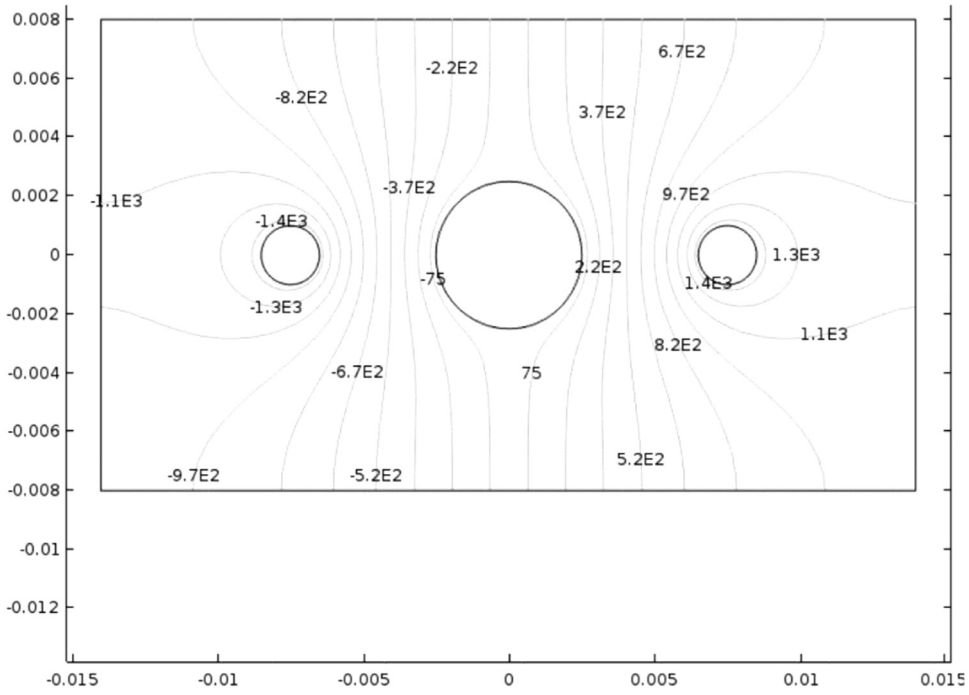

Fig. 5. Contour lines of the electric potential computed in Comsol™ for two needles and a stent in between. The unit at the equipotential lines is V; the unit on each axis is m.

ter. The default settings of Comsol have been used as detailed in Appendix B. A finer grid would probably result in reduced scatter and better agreement with the analytical that exactly satisfies the boundary condition at the stent. The electric potential field as computed with Comsol™ for this case is shown in Fig. 5. More numerical results with Comsol™ are given in Appendix B.

The boundary condition at the needles is not exactly satisfied by the choice V of (23) because of the thickness of the needles in this case, as discussed above directly under (23). This was further investigated by reflecting the monopoles at $z = \pm a^2/z_1$ into the needles. Similar to the solution (21), this yields a monopole with reduced strength at the center of the needle, where $z = z_1$, corresponding the last term on the RHS of (21), $[\ln(|1 - z_1/a|) - \ln(|1 - a/z_1|)]\ln(r)$, and a monopole at $z = z_1 - (D/2)^2/(z_1 - a^2/z_1)$. Because of the asymmetry, the monopole corresponding to the last term of the RHS of (21) is contributing and has a counterpart in the center of the needle at $z = -z_1$. With these reflection monopoles, the voltage at the needle surface is homogeneous to within 1 % for the case of Fig. 4.

The electric field near the stent is hardly affected by these reflection monopoles, whereas that near the needle is only slightly modified. The mean difference in the electric field at the points shown in Fig. 4, because of the reflection monopoles, is 4 %. However, for the much more realistic geometry of a needle diameter of 1 mm, a stent diameter of 5 mm and a z_1-value of 15 mm, the mean difference is only 0.5 %. The latter geometry will be used in the remainder of this study and since the points near the stent will be shown to be of main interest, the computations for the electric potential will be made without the reflection monopoles, *i.e.* with Eq. (24). The resulting inaccuracy is less than 0.5 % anywhere.

2.3. Heat production in a stent

During a pulse of arbitrary duration Δt, a quasi-steady situation occurs with electric current flowing through the tissue. The on and off switching of this current creates electromagnetic waves of various frequencies which may partly penetrate metals in the so-called skin depth. When a metal stent is positioned in between two pulsed electrodes, heat can therefore in principle be generated both in the tissue inside the stent and in the material of the stent itself. The heat generation will be quantified in this section, first for quasi-steady currents inside a fully metal stent, then for on and off switched currents in the stent itself and lastly for the tissue inside an open-structured stent.

2.3.1. Heat production in tissue inside a fully metal stent: quasi-steady currents

In Section 2.1 it was concluded that during typical IRE pulses, electric currents can be considered as stationary. This situation is considered below.

In electrostatics, the electric field can be derived from a potential, *i.e.* $\boldsymbol{E} = -\nabla\Phi$. At an interface between arbitrary volumes 1 and 2, $\boldsymbol{n}_2 \times (\boldsymbol{E}_1 - \boldsymbol{E}_2) = \boldsymbol{0}$ (Jackson [20], pg. 146) and $\boldsymbol{n}_2 \,.\, (\boldsymbol{D}_1 - \boldsymbol{D}_2) = q$, where q is a localized charge distribution that comprises both real charges and macroscopic excess charges (Jackson, [20], pg. 148). The boundary conditions at an interface between volumes 1 and 2 that do not contain charges, satisfying $\nabla.\varepsilon\boldsymbol{E} = 0$, then read: the normal component $\boldsymbol{n}_2 \,.\, \varepsilon\, \boldsymbol{E}$ is continuous and the components parallel to the interface, $\boldsymbol{n}_2 \times \boldsymbol{E}$, are also continuous.

The equations are similar for stationary electric currents in two media with homogeneous conductivities, σ_1 and σ_2: $\nabla.\sigma_i\, \boldsymbol{E}_i = 0$ (i = 1 or 2), $\boldsymbol{n}_2 \cdot\sigma_1\, \boldsymbol{E}_1 = \boldsymbol{n}_2 \cdot \sigma_2\, \boldsymbol{E}_2$ and parallel components $\boldsymbol{n}_2 \times \boldsymbol{E}$ must be continuous as well. Solutions from electrostatics hold for stationary currents provided conductivity, σ, replaces electric permittivity, ε.

The equations in magnetostatics are also similar for volumes with homogeneous permeability, μ. The magnetic field, $\boldsymbol{H}$, is derivable from a scalar potential then: $\boldsymbol{H} = -\nabla\Phi$ and magnetic induction, $\boldsymbol{B}$, is given by $\boldsymbol{B} = \mu\, \boldsymbol{H}$. Since

$$\mathbf{n}_2 \cdot (\mathbf{B}_1 - \mathbf{B}_2) = 0 \tag{25}$$

and, provided there are no currents, $\boldsymbol{n}_2 \times (\boldsymbol{H}_1 - \boldsymbol{H}_2) = 0$ [20, pg. 190], solutions from magnetostatics also hold for stationary currents provided conductivity, σ, replaces permeability, μ.

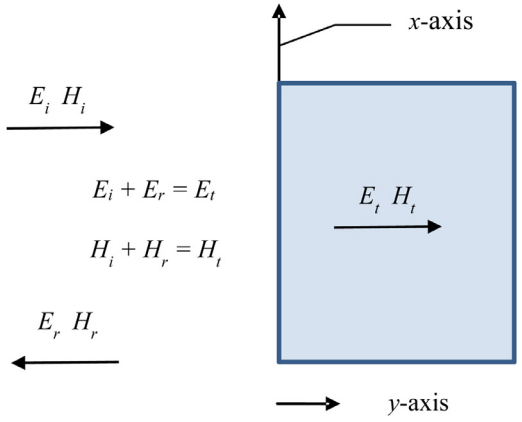

Fig. 6. Free after Fig. 3.14 of Sengupta and Liepa [23]. Points with y<0, to the left of the x-axis drawn, are in human tissue. Those with y>0 are inside a stent.

The latter similarity allows transferring the magnetostatics solution given by Jackson ([20], paragraph 5.12, pg. 199) for a spherical shell in a uniform field to that of a spherical shell with conductivity σ in a uniform electric field as created by two parallel flat plate electrodes. The reduction of the electric current inside the cavity in the shell is significant if the conductivity exceeds 10^3 S/m (Jackson, [20], pg. 201). More importantly, also the currents and heat production inside the shell itself can be computed. For stent radius $a = 2.5$ mm and stent thickness $b = 0.5$ mm, it is easily shown that the maximum heat production density in the shell itself is less than 1‰ of the heat production density in the uniform field imposed. This means that for all practical purposes the heat generation inside each shell *during* an electromagnetic pulse, so for quasi-steady currents, is negligible as compared to that outside the shell.

For points P inside a fully metal stent in these conditions we thus have no heat generation:

$$\sigma E(r,\theta)^2 = 0 \tag{26}$$

2.3.2. Heat production in the metal of a stent: on and off switched currents

Consider a tissue-metal interface, the *x,z* plane at y = 0, perpendicularly irradiated by an electromagnetic (EM) wave of radial frequency ω (Fig. 6). During the switching off and on of currents, electromagnetic waves penetrate the solid material of the stent in the so-called skin depth. This penetration is quantified below.

The incident, the reflected and the transmitted EM-fields are characterized by E_i, H_i (E oscillating in the x-direction, H in the direction normal to the plane of x and y directions), E_r, H_r and E_t, H_t, respectively. Using the notation that σ_1, σ_2 are the electric conductances of the tissue and the metal (σ_1 = 0.1-2 [21] versus $\sigma_2 = 10^6$ S/m, the latter for nitinol [22], an alloy of Nikkel and Titanium, often used for metal stents), μ_0, μ_1, μ_2 the magnetic permeability of vacuum ($\mu_0 = 4\pi\,10^{-7}$ Henry/m), and of tissue and metal, both about 1, $\varepsilon_0, \varepsilon_1, \varepsilon_2$ the dielectric permittivity of vacuum ($\varepsilon_0 = 8.854 \cdot 10^{-12}$ farad/m), and of tissue and metal, about 80 farad/m and several thousand farad/m, respectively. Maxwell's equations then give (*e.g.* Sengupta and Liepa, [23] pages 95, 96), with $j^2 = -1$ and omitting everywhere the factor $exp(j\omega t)$,

$$\mathbf{E}_i = \mathbf{x}E_i e^{-\gamma_1 y}\mathbf{E}_r = \mathbf{x}E_r e^{\gamma_1 y}\mathbf{E}_t = \mathbf{x}E_t e^{-\gamma_2 y} \tag{27}$$

$$\mathbf{H}_i = \mathbf{y}\frac{E_i e^{-\gamma_1 y}}{\eta_1}\mathbf{H}_r = -\mathbf{y}\frac{E_r e^{\gamma_1 y}}{\eta_1} \quad \mathbf{H}_t = \mathbf{y}\frac{E_t e^{-\gamma_2 y}}{\eta_2} \tag{28}$$

$$\gamma_1 = \sqrt{j\omega\mu_0\mu_1(\sigma_1 + j\omega\varepsilon_0\varepsilon_1)} \approx \sqrt{j\omega\mu_0\mu_1\sigma_1} \tag{29}$$

$$\gamma_2 = \sqrt{j\omega\mu_0\mu_2(\sigma_2 + j\omega\varepsilon_0\varepsilon_2)} \approx \sqrt{j\omega\mu_0\mu_2\sigma_2} \tag{30}$$

$$\eta_1 = \sqrt{\frac{j\omega\mu_0\mu_1}{\sigma_1 + j\omega\varepsilon_0\varepsilon_1}} \approx \sqrt{\frac{j\omega\mu_0\mu_1}{\sigma_1}}\ \eta_2 = \sqrt{\frac{j\omega\mu_0\mu_2}{\sigma_2 + j\omega\varepsilon_0\varepsilon_2}} \approx \sqrt{\frac{j\omega\mu_0\mu_2}{\sigma_2}} \tag{31}$$

The exceedingly small value of ε_0 causes that $\omega\varepsilon_0\varepsilon_{r1,2} \ll \sigma_{1,2}$ for tissue and nitinol for all radial frequencies relevant to a 0.1 ms IRE pulse, based on Fourier analysis of the pulse shape and on the amplitude. For example, requiring that $\omega\varepsilon_0\varepsilon_1 \ll \sigma_1$ implies that frequencies have to be much smaller than about $0.1/(8.85 \times 10^{-12} \times 80 \times 2\pi) \approx 2.2 \times 10^7$ Hz, well obeyed by a 0.1 ms pulse, i.e., frequencies $\lesssim 2.5 \cdot 10^5$ Hz. For nitinol this is a factor of about 10^7 larger ($\sigma_2 = 10^6$ S/m versus $\sigma_1 \approx 0.1$ S/m), or $\lesssim 2.5 \times 10^{12}$, thus much smaller than about 2.2×10^{14} Hz!

At the boundary (at $y = 0$), just inside the metal, continuity of the tangential components of $\boldsymbol{E}$ and $\boldsymbol{H}$ require boundary conditions

$$E_i + E_r = E_t H_i + H_r = H_t \tag{32}$$

or, from Eqs. 27–31,

$$\frac{E_i}{\eta_1} - \frac{E_r}{\eta_1} = \frac{E_t}{\eta_2}, \tag{33}$$

which give straightforwardly the following expression for E_t/E_i (Sengupta and Liepa [23], Eq. 3.252)

$$\frac{E_t}{E_i} = \frac{2\eta_2}{\eta_1 + \eta_2} \approx \frac{2\sqrt{\frac{\mu_2}{\sigma_2}}}{\sqrt{\frac{\mu_1}{\sigma_1}} + \sqrt{\frac{\mu_2}{\sigma_2}}} \approx 2\sqrt{\frac{\sigma_1\mu_2}{\sigma_2\mu_1}} = 2\sqrt{\frac{\sigma_1}{\sigma_2}} \approx (0.6 - 2.8) \cdot 10^{-3}. \tag{34}$$

Thus, the transmitted electric field into the nitinol metal is at most a few parts per 1000 of the incident field.

A 0.1 ms IRE pulse, for convenience considered having a top-hat shape, has a frequency spectrum from straightforward Fourier analysis of

$$E(\omega) = E_i \cdot \frac{2 \cdot \sin\left(\omega \cdot 5 \cdot 10^{-4}\right)}{\omega} \cdot e^{j\omega t} \quad \text{V/m}. \tag{35}$$

The temperature increase at the end of the IRE pulse with electric field E_t, at $t = \Delta t$, just inside the metal at the tissue-metal interface with metal mass density ρ_2, heat capacity c_2 and electrical conductivity σ_2, then becomes

$$\Delta T = \int_0^\infty d\omega \frac{\sigma_2 E_t^2(\omega)\Delta t}{\rho_2 c_2}. \tag{36}$$

This equation will be utilized in Section 3.3.

2.3.3. Electric field shielding by an open structure metal stent

The considerations of Section 2.3.1 were for fully closed metal stents. In addition, the electric field of open structured stent needs to be considered since it not necessarily needs to be zero inside the stent. The induced heating of the inside cavity of an open structured stent is therefore considered below.

Casey [24] analyzed the electromagnetic shielding of a metal wire mesh. For convenience, we use the geometry of a 2-dimensional metal wire mesh screen of wire diameter of $2r_w$ = 0.2 mm, mesh width 2 mm and a metal electrical conductance of $\sigma = 10^6$ S/m, the value for nitinol often used for metal stents [22]. The solution of the screening efficacy (named SE, in dB), defined as SE = -20 $\log_{10}(transmission)$, is given for a finite electric conducting metal in Casey's Fig. 6 as a function of the parameter $2R_s/Z_0$, with [24]

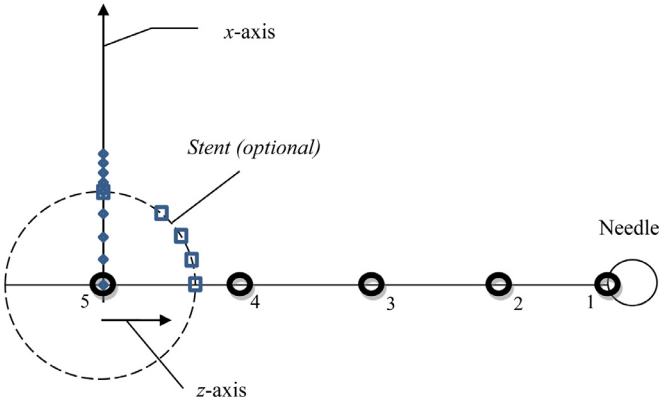

Fig. 7. Definition of numbers of points where temperature histories have been computed that will be shown and discussed here. The z-coordinates of points 1, 2, 3, 4 and 5 (thick circles) are respectively 14.5, 11.3, 7.5, 3.75 and 0 mm while they all have the same zero x-coordinate. The points on the stent surface (squares) have coordinates (z=2.5, x=0), (z=2.42, x=0.625), (z=2.16, x=1.25), (z=1.65, x=1.875) and (z=0, x=2.5) in mm. The 9 closed diamonds on the x-axis have x-coordinates 0, 0.65, 1.25, 1.875, 2.5, 2.75, 3.0, 3.25, 3.5 mm. Distance between centers of needle and stent, z_1 = 15 mm; stent radius is 2.5 mm; needle diameter, D, is 1 mm.

$$R_s = \frac{a_s}{\pi \cdot r_w^2 \cdot \sigma_2} = 0.063\Omega, \quad Z_0\sqrt{\frac{\mu_0}{\varepsilon_0}} = 377\Omega, \ \frac{2R_s}{Z_0} \approx 3.4 \cdot 10^{-4} \tag{37}$$

for $a_s = 2$ mm mesh separation, $r_w = 0.1$ mm radius of the wires, and $\sigma_2 = 10^6$ S/m. Thus, from Casey's Fig. 6, SE ≈ 70 dB, or from $SE \approx 70 = -20 \cdot \log_{10}(transmission)$ gives

$$transmission \approx 10^{-3.5} \approx 3.2 \cdot 10^{-4}, \tag{38}$$

even smaller than the amplitude ratio E_t/E_i of a full nitinol metal stent, Eq. (35). Note that the amplitude of the electric field at the inside of a full metal stent is less than E_t because of the damping by the exponential containing distance y in Eq. (27). In other words, nitinol metal stents reduce the incoming electric field by a factor of about a few times 10^{-4} and thus act as an effective Faraday cage. The inside of a hollow stent consisting of a wire mesh is therefore without noticeable heat production.

3. Results

3.1. Electric fields in tissue between two infinitely long electrodes

Typical electric field spatial distributions are shown in Fig. 4 and yield an E_i at the stent position of about $E_i \approx 0.4 \cdot 10^6$ V/m for 2 mm diameter electrodes, 1.25 cm inter-electrode distance and 3 kV power between the electrodes. For 1 mm electrode diameters, 3 cm distance and 3 kV, we find $E_i \approx 0.15 \cdot 10^6$ V/m. Thus, according to Eqs. (34), (38) the electric field transmitted to the nitinol metal surface, E_t, can vary between about

$$E_t \approx 50 - 1,100\,\mathrm{V/m}. \tag{39}$$

Further details about the electric field are provided by Fig.'s 4 and 5 and the figures in Appendix B.

3.2. IRE temperature field histories with and without a metal stent

Fig. 7 shows the labelling of points where temperatures will be considered. The dashed line centred at the origin represents the metal stent with radius $a = 2.5$ mm; computations both with and without the stent will be performed and discussed in this section. The stent is filled with similar tissue as the environment.

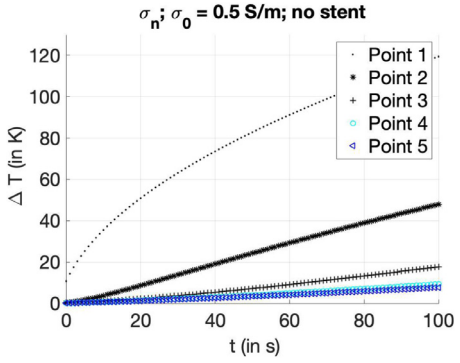

Fig. 8. Temperature increase histories at various distances from the origin (Fig. 7) without stent. Conductivity σ is a function of the number of pulses, Eq. (40); length z_1 = 15 mm; stent radius is 2.5 mm, 1500 V/cm; D = 1 mm; pulse duration = 0.1 ms; frequency f is 1 Hz.

The bioheat Eq. (11) is linear in ΔT so ΔT-responses to multiple pulses can be added as presented previously [10]. The computations are performed with the electrical conductivity depending on the number of IRE pulses, and hence on time, in the way found in [25] and applied to temperature calculations in [10]. First, we use that the electric conductance of the medium before the electric pulse, σ_0 S/m, increases during each IRE pulse, as shown by Ivorra et al. [25], approximately according to

$$\sigma_n/\sigma_0 \approx 1.29\sqrt{0.36\sqrt{n}+1} \tag{40}$$

where n denotes the nth pulse. Then, we use that the first pulse, at $t = 0$, yields $\Delta T^1(r, t = \Delta t \approx 0) = \Delta T^0(r, 0)\sigma_1/\sigma_0$ with $\Delta T^0(r, 0) = \sigma_0 E(r)^2 \Delta t/\rho c$, σ_0 the electric conductance before the electric pulse of duration Δt, and σ_1 the conductivity at the end of the first pulse. Just after the second pulse, say 1 s later, the first pulse reduces to $\Delta T^1(r, 1)\sigma_1/\sigma_0$. The second pulse gives $\Delta T^2(r, 0) \equiv \Delta T^0(r, 0)\sigma_2/\sigma_0$, thus proportional to the response of the first pulse at $t = 0$. Two pulses, at $t = 1$ s, thus cause $\Delta T(r, 1) = \Delta T^0(r, 0)\sigma_2/\sigma_0 + \Delta T^1(r, 1)\sigma_1/\sigma_0$, i.e., including the two responses to the *first* pulse at the two pulse events. Similarly, three pulses, at $t = 2$ s, give $\Delta T(r, 2) = \Delta T^0(r, 0)\ \sigma_3/\sigma_0 + \Delta T^1(r, 1)\sigma_2/\sigma_0 + \Delta T^2(r, 2)\sigma_1/\sigma_0$. Writing this as $\Delta T(r, 2) = \sum_{n=0}^{3-1} \Delta T^n(r, n)\sigma_{3-n}/\sigma_0$, gives with (14) after N consecutive pulses, frequency f, at time $t = (N-1)f^{-1}$ s:

$$\Delta T\left(r, (N-1)f^{-1}\right) = \sum_{n=0}^{N-1} \Delta T^n(r, n) \cdot \left(1.29\sqrt{0.36\sqrt{(N-n)}+1}\right) \tag{41}$$

The accumulated temperature increase computed with (41) at the locations shown in Fig. 7 is shown in Fig. 8 and subsequent figures in this section. The heat diffusivity is $\alpha = 1.4 \cdot 10^{-7}$ m^2/s and the thermal conductivity is initially $\lambda = 0.547$ W/(m. °C). Close to a needle the electric potential changes rapidly over small distances and the electric field is strong. At point 1 the temperature change after 100 pulses is therefore exceeding 120°C, see Fig. 8. It is the only location of the 5 shown where already after one single pulse the temperature change is notable. Halfway the two needles, at point 5, the electric field and hence the dissipation rate and temperature rise are smallest after 100 pulses. This is the situation where a stent is absent (Fig. 8).

The effect of the stent with a diameter five times as big as that of the needle is shown in Fig. 9 that zooms in at the points 2-5, see Fig. 7. The LHS of Fig. 9 contains the same data as shown in Fig. 8. With a stent, the RHS, the origin (point 5) only starts warming up after about 10 s since no electric field is generated

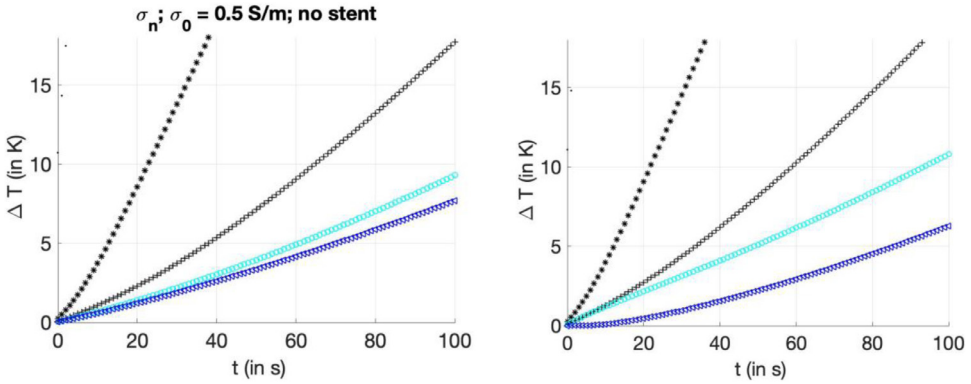

Fig. 9. Temperature increase histories at locations 2 – 5 without stent (left) and with stent (right). Legend is the same as in Fig. 8. Conductivity σ is a function of the number of pulses, Eq. (40), and other data are the same as in Fig. 8.

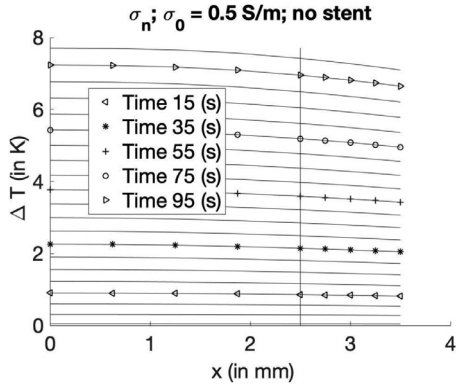

Fig. 10. Temperature profiles after one pulse (lowest line) and at times 5, 10, 15, …, 100 s, after respectively 5, 10, 15, and …, 100 pulses at 1 Hz. The line at x = 2.5 mm is to guide the eye and indicates where the stent edge would be if the stent were present. Locations correspond to the diamonds of Fig. 7.

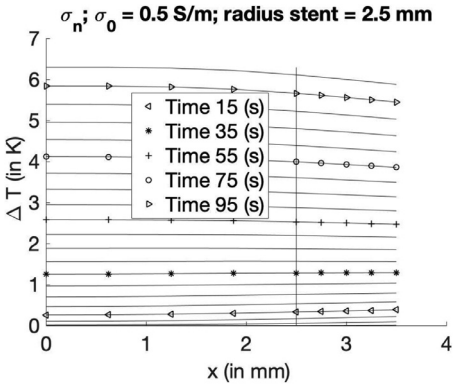

Fig. 11. As Fig. 10 but with stent present. The profile after one pulse is barely notable near x = 3.5 mm.

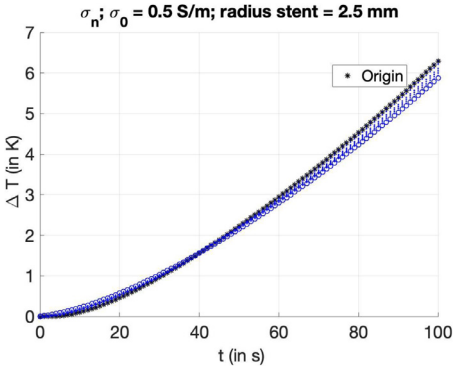

Fig. 12. Time histories of the temperature increase at the locations used in Fig. 11, indicated by diamonds in Fig. 7; the origin is starred, the top location with x-coordinate 3.5 mm has an open circle. Same conditions as in Fig. 11.

inside the stent. Heat must diffuse from outside the stent to the inside. The typical diffusion time, *t*, is easily estimated by putting the Fourier number, Fo = $\alpha\ t^2/(2a)^2$, equal to 1, with α the heat diffusivity $1.4 \cdot 10^{-7}$ m^2/s and *a* the radius of the stent, 2.5 mm; the result is 10 s indeed. Our experimental finding [12, page 4] that similar maximum temperatures were reached in no-stent-IRE as in stent-IRE concerned a location at a stent with a diameter of 5 mm and a time delay of 10 to 20 s. This agrees with the above finding and the Fourier criterion estimation.

Points 3 and 4 correspond to the lines of crosses and circles and exhibit a faster temperature rise than without a stent, see Fig. 9. The electric field at these points is increased by the introduction of the stent because the field line through points 3 and 4 stands perpendicular to both stent and needle and is considerably shorter with stent than without stent. This explains the faster rise in temperature with stent at these places.

The points indicated by diamonds on the x-axis in Fig. 7 exhibit temperature histories shown in Fig. 10. Point 5 at the origin has the highest increase in temperature after 100 pulses at 1 Hz. The farther away from the origin, the weaker the electric field and the smaller the temperature increase are, but differences remain within 1 ^{0}C after 100 s.

This is drastically changed by the introduction of a stent, see Fig. 11. At times until about 40 s, 40 pulses, temperature differences generated outside the stent exceed those at the inside, see e.g the line at 15 s. At later times, the origin inside the stent experiences the highest temperature increase because of diffusion of heat from the two sides that face a needle; at one side point 4 in Fig. 7 is located, for example. The change of trend at about 40 s is more clearly shown in Fig. 12. Initially, the origin does not rise in temperature, but this changes after about 10 s for thermal diffusion reasons discussed above, Fig. 9B. At times exceeding 60 s, on the contrary, the temperature at the origin is clearly highest of all for a reason that is discussed below.

The explanation for the above change of trend at about 40 s is the fact that more heat is generated at the sides of the stent facing the needles than at the top of the stent. This is further examined by studying the history of the temperature profile at the circumference of the stent, see Fig. 13. At 35 s and 55 s the temperature increase at *x=0*, which is near point 4 in Fig. 7, is clearly seen to be higher with stent (figure on the right) than without (left fig-

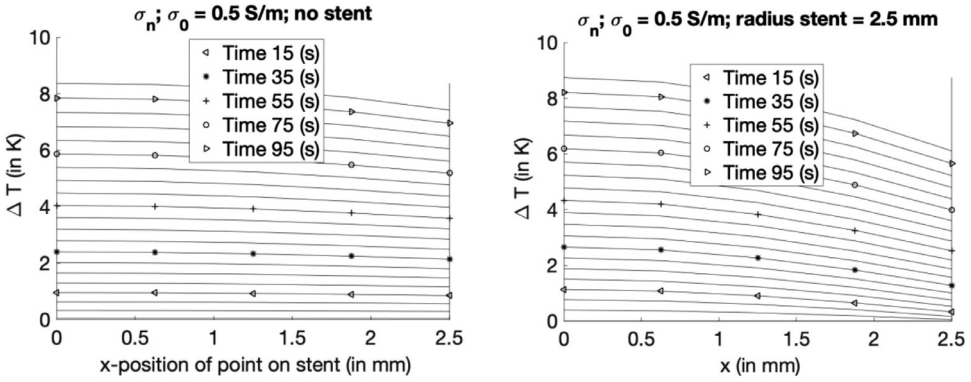

Fig. 13. Temperature profiles at the circumference of the stent, the locations indicated by squares in Fig. 7. Profiles are drawn at subsequent times with stent (figure on the right) and without stent (left figure).

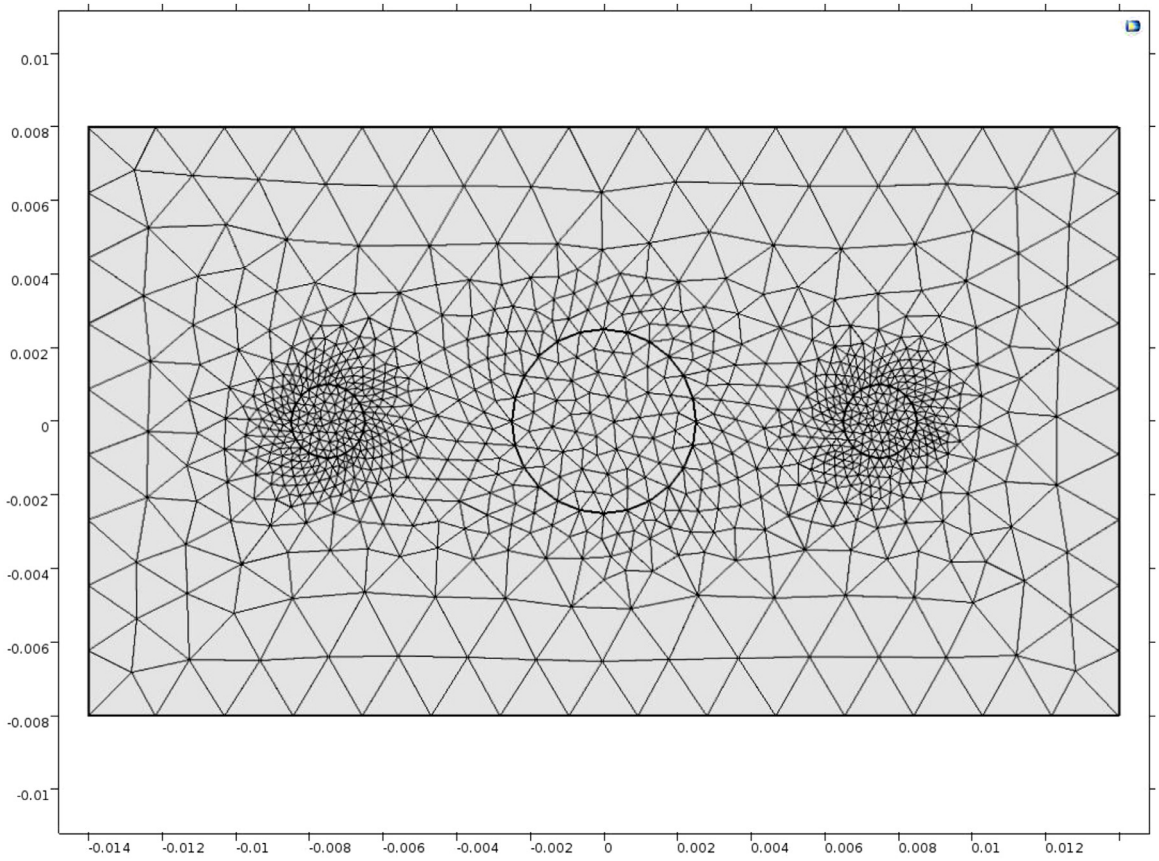

Fig. 14. Computational mesh applied for 2D computations in Comsol™. The unit on both axes is m.

ure). The surplus of heat generated near point 4 diffuses away to the inside of the stent, which reduces the difference in temperature between with and without stent at later times at $x=0$. At the top of the stent, the point where $x=2.5$ mm and that is farthest away from the needles, the heat generation with stent is clearly less than that without stent, always. The electric field lines must stand perpendicular to the stent surface, which creates long field lines to the needles at this point of the stent. Consequently, the electric field and the energy dissipation rate are smaller on top of the stent than at the sides of the stent that are facing the needles. The stent creates cold spots on the sides of the stent that are farthest away from the needles by lengthening the electric field lines there.

In addition, the stent acts as a heat sink. The heat sink action is the fact that the energy dissipated near the stent during a pulse diffuses away during the time in between two pulses to the volume inside the stent. The heat sink action of the stent and the creation of cold spots at the sides not facing the needles are precisely the reason why a viable rim around the stent has been observed in pig experiments [13]. The temperature spot II in this reference [13] has the lowest temperatures measured and corresponds to the location *(z=0, x=2.5)* where the lowest temperatures are computed (Fig. 13). Although in the experiment the gel was shaped as a slab with limited thickness, whereas in the computations the fluid outside the stent is unlimited, the mechanisms of heat sink action and diffusion of heat are the same.

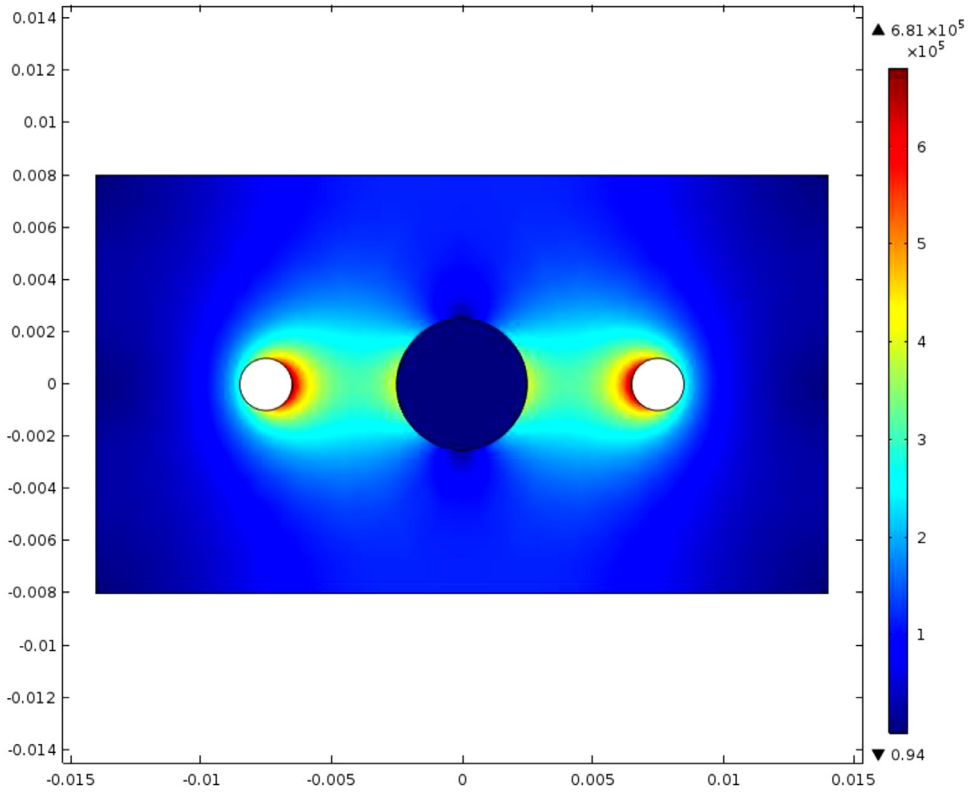

Fig. 15. The norm of the electric field corresponding to Fig. 5. The unit at the color bar is V/m; the unit on each axis is m.

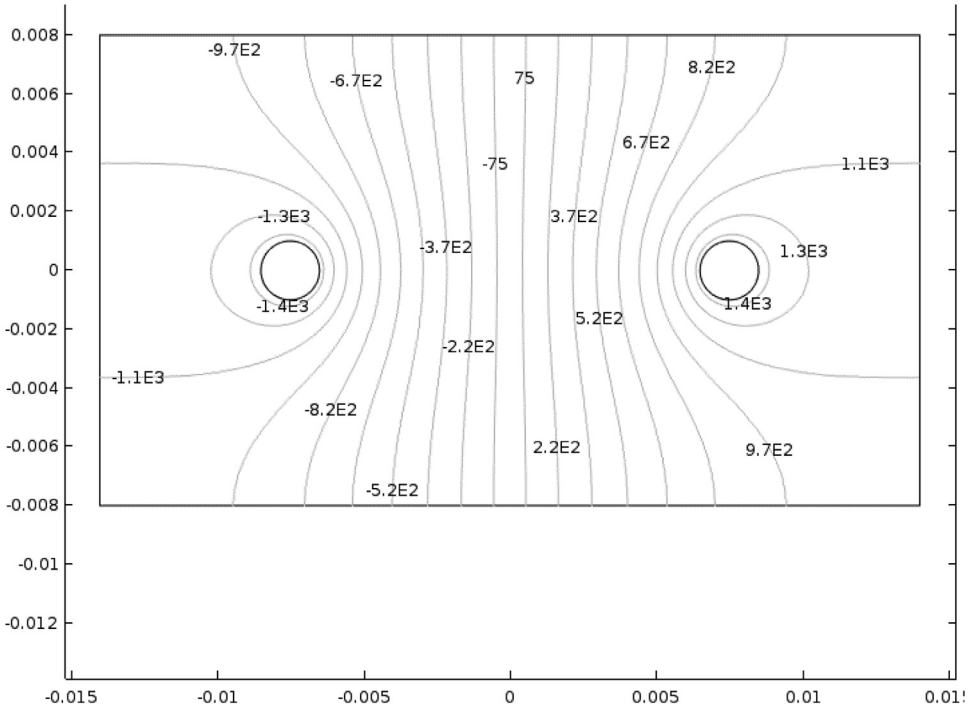

Fig. 16. Contour lines of the electric potential computed in Comsol™ for two isolated needles. The unit at the equipotential lines is V; the unit on each axis is m.

3.3. Temperature calculation in the metal at a tissue-metal junction

Using the electric fields generated by a short $\Delta t = 0.1$ ms IRE pulse, we estimate the temperature effects in a metal block with the electrothermal physical properties of nitinol to represent the stent and applying that temperature rise $\Delta T(\omega) = \sigma_2 E_t^2(\omega)\Delta t/\rho c$ for a short (0.1 ms) electric field pulse of strength $E_t(\omega)$, Eq. (27). We have to integrate this equation over all frequencies and their Fourier amplitudes, Eq. (36). We used average values for density ($6.7 \cdot 10^3$ kg/m^3) and heat capacity ($0.5 \cdot 10^3$ J/kg/^{0}C) found for Ni and Ti, because we could not find these data for nitinol. By using the maximum E-field of 1,100 V/m, i.e. the maximum field at the

inside metal boundary, Eq. (28), we estimate the maximum temperature effect here as

$$\Delta T=\int_0^\infty d\omega\frac{\sigma_2 E_t^2(\omega)\Delta t}{\rho_2 c_2}=\frac{\sigma_2 E_t^2(0)\Delta t}{\rho_2 c_2}\int_0^\infty d\omega\frac{E_t^2(\omega)}{E_t^2(0)}=\frac{10^6\cdot\left(1.1\cdot10^3\right)^2\cdot10^{-4}}{\left(6.7\cdot10^3\right)\cdot\left(0.5\cdot10^3\right)}\int_0^\infty d\omega\cdot\frac{4\cdot\sin^2\left(\omega\cdot5\cdot10^{-5}\right)}{\omega^2}$$
$$=\frac{4\cdot10^6\cdot(1.2)\cdot10^6\cdot10^{-4}\cdot\left(5\cdot10^{-5}\right)}{\left(6.7\cdot10^3\right)\cdot\left(0.5\cdot10^3\right)}\int_0^\infty d\left(\omega\cdot5\cdot10^{-5}\right)\frac{\sin^2\left(\omega\cdot5\cdot10^{-5}\right)}{\left(\omega\cdot5\cdot10^{-5}\right)^2}=7.2\cdot10^{-3}\cdot\frac{\pi}{2}\approx10^{-2}{}^{\circ}\mathrm{C}. \tag{42}$$

Thus, even for a 1 cm electrode distance and 3 kV, the temperature effect of a 0.1 ms IRE pulse in a block of metal with a position-independent maximal electric field is negligible. For the 1.5 cm electrode distance, the maximum temperature increase is about 0.0016 ^{0}C. In other words, the electric field calculated at the position of a 5 mm diameter metal stent, caused by an IRE pulse of 0.1 ms, 3 kV and 1 – 1.5 cm electrode distance, does not noticeably heat up a metal block with the electrothermal physical properties of nitinol. Thus, 100 such IRE pulses will not significantly influence the temperature distribution inside the stent either.

4. Conclusions

We have shown that a metal stent will not be noticeably heated up by pulses applied in clinical irreversible electroporation, a counterintuitive result that required application of Maxwell's equations to the tissue-stent configuration. The Faraday cage functions well, and heating of the stent is merely by conduction from the ambient tissue, as high-frequency heat production close to the stent by Fourier frequencies and their amplitudes of the pulse shape is very small. This conclusion is of major significance because (i) it shows that it is safe to apply IRE therapy in the presence of a metal stent, and (ii) it prevents stent removal and thus also surgical complications.

Major trends of temperature field histories found in thermal camera experiments [12,13] have been explained with straightforward simplifications of the electric field generated by two needles in tissue surrounding a stent and by subsequent modeling of the heat generation and transport of heat with the bio-heat equation. Close to the needles, gradients in the electric field and hence energy dissipation rate and temperature rise are highest. However, during the time with zero electric field after each pulse this heat mostly diffuses away, by conduction, to other places. At the sides of a stent, positioned in between two needles, that are not facing the needles, temperatures in a typical run of 100 s remain lower as compared to the situation without stent. This creation of cold spots in combination with the action of a stent as a heat sink explains the low temperature rim around the stent found experimentally in pig experiments [12,13].

Declaration of Competing Interest

The authors declare that they have no known competing financial interests or personal relationships that could have appeared to influence the work reported in this paper.

Appendix A

Expression of the heat production by two point-charges

Angle φ is defined as the angle between $\hat{r}_1$ and $\hat{r}_2$ (Fig. 1). With the cosine rule for φ, *i.e.*, $cos\varphi=[r_1^2+r_2^2-(2z_1)^2]/(2r_1r_2)$, and with the cosine rules of position angle θ (Fig. 1) and of complementary angle $(\pi-\theta)$, and with $cos\theta=-cos(\pi-\theta)$, the following equation is derived:

$$cos\theta=\frac{z_1^2+r^2-{r_1}^2}{2z_1r}=-cos(\pi-\theta)=-\frac{z_1^2+r^2-{r_2}^2}{2z_1r}. \tag{A1}$$

With some algebra (A1) directly yields $(r_1^2+r_2^2)=2({z_1}^2+r^2)$. So, for angle φ

$$cos\,\varphi=\left[2({z_1}^2+r^2)-(2z_1)^2\right]/(2r_1r_2)=\left[r^2-{z_1}^2\right]/(r_1r_2) \tag{A2}$$

and energy dissipation rate can be expresses as follows:

$$\sigma E(r,\theta)^2=\frac{\sigma Q^2}{(4\pi\varepsilon_0)^2}\left[\frac{\hat{r}_1}{r_1^2}-\frac{\hat{r}_2}{r_2^2}\right]^2=\sigma\left(\frac{Q}{4\pi\varepsilon_0}\right)^2\cdot\left[\frac{1}{r_1^4}+\frac{1}{r_2^4}-\frac{2\left(r^2-{z_1}^2\right)}{r_1^3r_2^3}\right]. \tag{A3}$$

Eq. (A3) expresses the volumetric heat production at $P(r,\theta)$ caused by 2 electric point charges $+Q$ and $-Q$, at distances $-z_1$ and z_1 from the origin (Fig. 1), at arbitrary location (r,θ) in polar coordinates.

Appendix B

Computation settings in Comsol™

This appendix summarizes the governing equations, initial and boundary conditions used for the finite element computations with Comsol Multiphysics™ 5.2.1.152 and gives typical results and values of physical constants used. Fig. 14 shows the geometry of three cylinders with parallel axis perpendicular to the plane as well as the mesh applied.

The specific electric conductivity, σ, and the relative permittivity, ε_r, are material properties. Their values are 0.1 S/m and 80, respectively, for the fluid (representing human body tissue) that occupies the entire region outside of the needles. In the computations presented in this paper the interior of the stent, represented by the cylinder at the centre of Fig. 14, was also filled with this fluid. In other computations the stent was taken to be solid steel with σ = 4,032.10^6 S/m and ε_r = 1 and with a mass density, ρ, of 7850 kg/m^3, a heat capacity, c, of 475 J/(kg.^{0}C) and a heat conductivity coefficient, λ, of 44,5 W/(m.^{0}C). This is the material that the stent and the needles are typically made of. The mass density of the fluid is 1000 kg/m^3, while its c = 4100 J/(kg.^{0}C) and λ = 0,5908 W/(m.^{0}C). For the computation of the electric field the interior of the stent is inessential as the boundary condition on the stent is that the tangential component of the electric field is zero, *i.e.* that the stent surface has a constant electric potential, Φ. This value is zero in the computations with Comsol™. The imposed voltages at the surfaces of the needles, where also the boundary condition of a constant potential had to be satisfied, were in most computations taken to be + 1500 V and -1500 V. The electric field at the outer boundary of the computation domain in Fig. 14 satisfies the boundary condition that the normal component of the electric field is zero. Since in the analytical solution this condition is only satisfied at infinity, a comparison with predictions of Comsol™ can only be made for the central region at relatively large distance from the outer boundaries. For this reason, the comparison with the analytical solution is only applied to the area in between the needles and the stent (Fig. 4). The results below will show that the electric field there is only marginally affected by the boundary condition at the outer boundary of the computational domain. Doubling the domain gave changes in the electric field in between the needles and the stent that were far less than the scatter in the computed points of Fig. 4.

There are no remnant displacements of currents and therefore the total electric field including polarization $\boldsymbol{D}$, is given by $\boldsymbol{D}=\varepsilon_0\,\varepsilon_r\,\boldsymbol{E}$, with ε_0, the permittivity in vacuum, equal to 8.854 10^{-12} farad/m and $\boldsymbol{E}$ the electric field vector without polarization. There are no externally generated currents and the electric current $\boldsymbol{J}$, therefore satisfies the following equation:

$$\mathbf{J}=\sigma\mathbf{E}+\partial\mathbf{D}/\partial t. \tag{B1}$$

In quasi-steady conditions the following equations hold

$$\mathbf{J} = \sigma \mathbf{E} \tag{B2}$$

$$\nabla . \mathbf{J} = 0 \tag{B3}$$

The applicability of quasi-steady conditions to the conditions that determine the electric field is proven in the main text, in Sections 2.1.1, 2.3.2 and 3.3. Because the conditions are quasi-steady, there was no need to solve for the magnetic field.

For a homogeneous electric conductivity, the last equation of a divergence-free current in combination with the defining equation of the electric potential, Φ :

$$\mathbf{E} = -\nabla \Phi \tag{B4}$$

yield the Laplace equation for the potential Φ:

$$\nabla . \nabla \Phi \ = 0. \tag{B5}$$

The electromagnetic heat source, $\sigma E^{\,2}$, which is energy dissipation rate density in W/m³, couples the electric field to the energy equation:

$$\rho \, c \, \partial T / \partial t + \sigma c \mathbf{u} . \nabla \ T = \sigma E^2 + \nabla \lambda . \nabla T \tag{B6}$$

The fluid velocity, $\boldsymbol{u}$, is zero in all cases of this study and λ is taken to be homogeneous. The initial temperature condition prescribes a constant temperature everywhere. At the outer boundary of the computation domain, the temperature gradient is assumed to have a zero-component normal to the boundary. This implies that there are no energy losses from the computational domain. This boundary condition is of course only relevant for the computation of the temperature by Comsol™ and such computations are not presented in this paper.

Computations have been performed in Comsol™ with 7128 degrees of freedom. A computation time of 5 s and a virtual memory of 1.71 GB sufficed to solve for the electric field and the temperature field simultaneously during 0.1 ms. Computations of temperature histories, not shown in this paper, were obtained with the aid of a variable-order, variable-step-size backward Euler time differentiation with order varying between 1 and 2 and with 0.001 fraction of the initial step for the backward Euler computation. The absolute tolerance was 0.001 and the variables, the electric potential and the temperature, were scaled. During the physical time 0.1 ms the electric potential remained as shown in Fig. 5.

Fig. 5 shows that the boundary conditions of the electric field are satisfied. Fig. 15 gives the corresponding electric field.

For comparison with Fig. 5, Fig. 16 gives the electric potential in the absence of a stent.

References

[1] D.C. Chang, T.S. Reese, Changes in membrane structure induced by electroporation as revealed by rapid-freezing electron microscopy, Biophys. J. 58 (1990) 1–12.

[2] E.W. Lee, D. Wong, S.V. Prikhodko, A. Perez, C. Tran, C.T. Loh, S.T. Kee, Electron microscopic demonstration and evaluation of irreversible electroporation-induced nanopores on hepatocyte membranes, J. Vasc. Interv. Radiol. 23 (2012) 107–113.

[3] B. Rubinsky, G. Onik, P. Mikus, Irreversible electroporation: a new ablation modality-clinical implications, Tech. Cancer Res. Treat. 6 (2007) 37–48.

[4] R.V. Davalos, S. Bhonsle, R.E. Neal, Implications and considerations of thermal effects when applying irreversible electroporation tissue ablation therapy, Prostate 75 (2015) 1114–1118.

[5] M.J.C. van Gemert, P.G.K. Wagstaff, D.M. de Bruin, T.G. van Leeuwen, A.C. van der Wal, M. Heger, C.W.M. van der Geld, Irreversible electroporation: just another form of thermal therapy? Prostate 75 (2015) 332–335.

[6] P. Agnass, E. van Veldhuisen, M.J.C. van Gemert, C.W.M. van der Geld, K.P. van Lienden, T.M. van Gulik, M.R. Meijerink, M.G. Besselink, H.P. Kok, J. Crezee, Mathematical modeling of the thermal effects of irreversible electroporation for *in vitro, in vivo*, and clinical use: a systematic review, Int. J. Hyperthermia 37 (1) (2020) 486–505, doi:10.1080/02656736.2020.1753828.

[7] M. Faroja, M. Ahmed, L. Applebaum, E. Ben-David, M. Moussa, J. Sosna, I. Nissenbaum, S.N. Goldberg, Irreversible electroporation ablation: is all the damage nonthermal? Radiology 266 (2) (2013) 462–470.

[8] E.M. Dunki-Jacobs, P. Philips, R.C.G. Martin II, Evaluation of thermal injury to liver, pancreas and kidney during irreversible electroporation in an *in vivo* experimental model, Br. J. Surg. 101 (2014) 1113–1121.

[9] P.A. Garcia, R.V. Davalos, D. Miklavcic, A numerical investigation of the electric and thermal cell kill distributions in electroporation-based therapies in tissue, PLoS One 9 (8) (2014) e103083 1-12.

[10] P.G.K. Wagstaff, D.M. de Bruin, W. van den Bos, A. Ingels, M.J.C. van Gemert, P.J. Zondervan, R.M. Verdaasdonk, K.P. van Lienden, T.G. van Leeuwen, J.J.M.C.H. de la Rosette, M.P. Laguna-Pes, Irreversible electroporation of the porcine kidney: temperature development and distribution, Urol. Oncol. 33 (2015) 168.e1–168.e7.

[11] M. Heger, A.C. van der Wal, G. Storm, M.J.C. van Gemert, Potential therapeutic benefits stemming from the thermal nature of irreversible electroporation of solid cancers, Hepatobil. Pancr. Dis. Intern. 14 (2015) 331–333.

[12] W. van den Bos, H.J. Scheffer, J.A. Vogel, P.G.K. Wagstaff, D.M. de Bruin, M.G.H. Besselink, M.J.C. van Gemert, J.J.M.C.H. de la Rosette, M.R. Meijerink, J.H. Klaessens, R.M. Verdaasdonk, Thermal energy during irreversible electroporation and the influence of different ablation parameters, J. Vasc. Intervent. Radiol. 27 (3) (2016) 433–443.

[13] H.J. Scheffer, J.A. Vogel, W. van den Bos, R.E. Neal II, K.P. van Lienden, M.G.H. Besselink, M.J.C. van Gemert, C.W.M. van der Geld, M.R. Meijerink, J.H. Klaessens, R.M. Verdaasdonk, The influence of a metal stent on the distribution of thermal energy during irreversible electroporation, PLoS ONE 11 (2) (2016) e0148457 1-13.

[14] C.-Y. Hsiao, K.-W. Huang, Irreversible electroporation: a novel ultrasound-guided modality for non-thermal tumor ablation, J. Med. Ultrasound 25 (2017) 195–200.

[15] J. Fainberg, B.A.A. Awamleh, A.P. de Rosa, G. Chesnut, T. Lee, B.A. Ehdaie, Contemporary systematic review of partial prostate gland ablation outcomes: a comparative study of thermal versus non-thermal technologies, J. Urol. 201 (4Supplement) (2019) e1150 Abstract MP78-19.

[16] C. Månsson, A. Nilsson, B.-M. Karlson, Severe complications with irreversible electroporation of the pancreas in the presence of a metallic stent: a warning of a procedure that never should be performed, Acta Radiol. Short Rep. 3 (11) (2014) 1–3.

[17] Comment to H.J. Scheffer, J.A. Vogel, W. van den Bos, M.R. Meijerink, M.G.H. Besselink, R.M. Verdaasdonk, J. Klaessens, C.W.M. van der Geld, M.J.C. van Gemert, C. Månsson, A. Nilsson, B.-M. Karlson, Severe complications with irreversible electroporation of the pancreas in the presence of a metallic stent: a warning of a procedure that never should be performed, Acta Radiol. Short Rep. 3 (11) (2014) 1–3. Acta Radiologica Open 4 (7) (2015) DOI: 10.1177/2058460115584111 1-3.

[18] C. Månsson, A. Nilsson, D. Månsson, B.-M. Karlson, Response from the authors of the original article, Comment to: Månsson C, Nilsson A, Karlson B-M. Severe complications with irreversible electroporation of the pancreas in the presence of a metallic stent: a warning of a procedure that never should be performed, Acta Radiol. Open 3 (11) (2014) 1–3 Acta Radiologica Short Reports 4 (10) 2015 1-2.

[19] K.D. Cole, J.V. Beck, A. Haji-Sheikh, B. Litkouhi, in: Heat Conduction using Greens Functions, 2nd Ed., Taylor and Frances, 2011, pp. 167–176.

[20] J.D. Jackson, in: Classical Electrodynamics, 3rd Ed., John Wiley & Sons, Hoboken, NJ, 1999, pp. 146–148.

[21] C. Gabriel, A. Peyman, E.H. Grant, Electrical conductivity of tissue at frequencies below 1 MHz, Phys. Med. Biol. 54 (2009) 4863–4878.

[22] H.U. Schuerch, Certain physical Properties and Applications of Nitinol, November 1968 NASA CR-1232.

[23] D.L. Sengupta, V.V. Liepa, in: Applied Electromagnetics and Electromagnetic Compatibility, Wiley, 2005, pp. 95–96.

[24] K.F. Casey, Electromagnetic shielding behavior of wire-mesh screens, IEEE Trans. Electromagn. Compat. 30 (1988) 298–306.

[25] A. Ivorra, B. Al-Sakere, B. Rubinsky, L.M. Mir, In vivo electrical conductivity measurements during and after tumor electroporation: conductivity changes reflect the treatment outcome, Phys. Med. Biol. 54 (2009) 5949–5963.